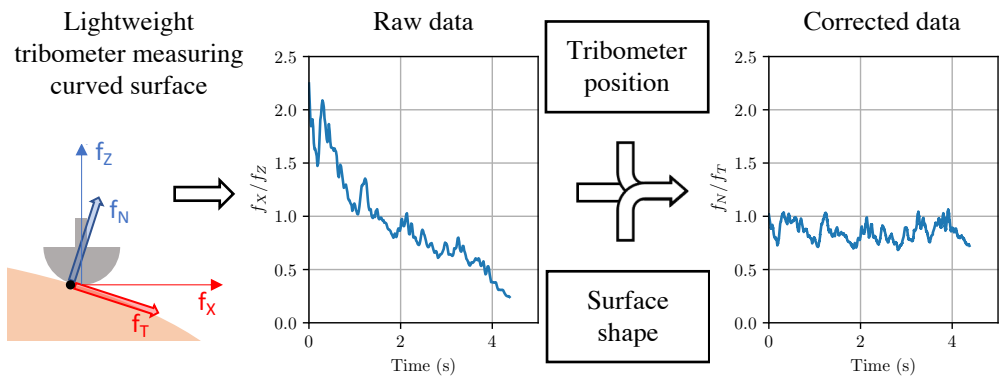


Graphical Abstract

In situ measurement of friction on curved surfaces

Pearson A. Wyder-Hodge, Egor Larionov, Dinesh K. Pai



Highlights

In situ measurement of friction on curved surfaces

Pearson A. Wyder-Hodge, Egor Larionov, Dinesh K. Pai

- Propose a general method to measure force data on curved surfaces for sliding contacts and friction analysis.
- Implement this curve correction method with a linear sliding handheld tribometer.
- Describe the importance of carefully testing and calibrating the outputs of lightweight devices that may have low flexural rigidity.

In situ measurement of friction on curved surfaces

Pearson A. Wyder-Hodge^{a,*}, Egor Larionov^a and Dinesh K. Pai^{a,b}

^aUniversity of British Columbia, 2329 West Mall, Vancouver, BC Canada V6T 1Z4

^bVital Mechanics Research, Vancouver, BC Canada

ARTICLE INFO

Keywords:

Friction

Measurement

Sliding

Topography

ABSTRACT

In situ measurement of frictional properties, particularly of human skin, is challenging. A major challenge is that the measured surface may be curved and oriented arbitrarily relative to the measurement device, making it difficult to obtain accurate and reliable friction estimates.

Here we propose a method to simultaneously estimate the orientation of the surface during friction measurements, using a custom-made hand-held tribometer. The method accounts for the position and orientation of the tribometer relative to the shape of the measured surface. Our simple calibration method allows lightweight tribometers to be built with cheaper materials like plastic, without sacrificing accuracy.

1. Introduction

Accurately and reliably measuring friction between human skin and contacting surfaces is a prerequisite to understanding the mechanics of skin friction. In turn, this allows designers and engineers to optimize the comfort and usability of the surfaces that frequently come into contact with our skin. Several areas of interest rely on accurate measurements: clothing [15, 4], wearable devices [28], computer simulation [22, 23], skincare [31, 32], cosmetics [33], aging [5, 39], injuries and scarring [2, 24], and sensation [11, 20]. When designing sportswear, it is important to limit the amount of friction that is experienced by the wearer, as it may cause discomfort or even pain [9]. Clinically, reducing the friction between the skin of bedridden hospital patients and fabric can reduce pressure injuries, such as blisters and abrasions [13, 29]. Despite the the interest in this type of data, methods for measuring skin friction across the body have fallen short.

Classically, in vivo research of skin friction has predominantly investigated easy-to-access areas on the body, such as the hand and the forearm [7]. However, it is known that friction varies across anatomical locations [5, 6, 38, 39, 16]. In order to efficiently and accurately measure friction across the body, several factors need to be accounted for. First, the tribometer should be mobile so that the device can easily be moved to access hard-to-reach areas (e.g. chest, back, and face). Second, the measurement system needs to account for the surface shape of the body so that the forces essential for analyzing friction, the normal (f_N) and tangent forces (f_T or force of friction), are recorded correctly. This problem is not trivial, as the human body is curved and these curves vary between humans. Third, the movement of the contact should be representative of the application; sliding contacts are more common than rotating contacts in everyday life. Finally, the measurement strategy should minimize any transient changes to the skin during measurement. For example, if the skin is occluded by the tribometer in one location

for too long then the moisture level may increase, causing changes in the measured forces. [7]

Common skin friction measurement techniques can be organized into four categories: the contacting surface rotates with the axis of rotation perpendicular to the skin [5, 16, 10, 39], rotates with the axis of rotation parallel to the skin [35], slides linearly across a distance of the skin while the skin stays in place [21, 3, 1, 36], or the skin patch slides across a stationary force sensor [8, 12, 34, 37, 17]. Rotating tribometers are often portable and handheld. The portability allows for rapid data collection from many different locations and hard-to-reach areas on the body [5, 16, 10]. This is an advantage over the linear sliding tribometers, which are not portable and require anatomical locations that can be easily placed on a sampling stage (e.g. forearm [19, 21, 3, 1], fingers [30], and calves [25, 24]).

To calculate the coefficient of friction (COF) between two surfaces it is necessary to reliably measure the surface normal and the surface tangent in the direction of motion during the contact. The measurement device needs to be aligned correctly with the skin surface to ensure that the forces measured by the tribometer are representative of the f_N and f_T . Most linear sliding tribometers restrain the region of interest so that the probe tip is properly aligned along a flat skin surface. Rotating tribometers do not move across the curves of the body, as they are held in a single location while the head of the probe rotates.

Two advantages of linear sliding tribometers are that they collect data that is more representative of everyday skin contacts and researchers do not have to be as concerned about the variability of skin conditions from occlusion during measurement. In the literature linear sliding tribometers are used more often than rotating tribometers. Nevertheless, there remains an absence of linear sliding measurements on the hard-to-access areas, due to constraints from the sampling stage and curvature of the regions of interest.

Here, a method is proposed to reliably estimate f_N and f_T across curved surfaces with a custom-made tribometer (Fig. 1). This is done by accounting for the position and rotation of the tribometer relative to the known shape of the

*Corresponding author
ORCID(s):

measurement target's surface. This setup can align the frame of the measured forces to the contact frame to account for any misalignment between the two during measurement. In addition, this device allows for linear measurements while being mobile. The proposed surface correction method is tested by taking linear sliding force measurements across various curved surfaces of skin like silicone.

While the construction of our tribometer is structurally sound, like many lightweight devices it is encased in plastic, and is not completely rigid or isotropic in its stiffness. Furthermore, the displacement of the probe tip from the force sensor amplifies this discrepancy. Therefore, this is a representative example to demonstrate the importance of carefully testing and calibrating the output from a custom-made measurement device. Fig. 2 shows measurements from a constant force applied 360° about the probe. The asymmetry is clearly visible in the output, where the forces are expected to be constant. A calibration scheme is developed here to account for potential biases when measuring friction in different directions with respect to the probe frame. This scheme allows for reliable friction sensors to be built with cheaper materials like plastic without sacrificing accuracy.

2. Methods

2.1. Skin probe

A custom skin probe [27] (Fig. 1) is used to collect force and position data during sliding contacts. The probe contains a six-axis force/torque sensor (F/T Nano 17, ATI Industrial Automation, USA) connected to a carbon fiber shaft (Alston Carbon Fiber Tech Co., China) with a 3D printed (Ultimaker 3, Netherlands) spherical probe tip (radius = 3.5 mm) at the end of the shaft. A 10-camera motion capture system (Vicon, Oxford, UK) tracks the position and orientation of 5 retro-reflective markers strategically attached to the probe to avoid occlusion from the arm of the experimenter. Through calibration, the weight of the shaft on the force sensor is accounted for and the forces at the force sensor frame are transformed to the probe tip frame defined by $\tilde{\mathbf{f}} = (\tilde{f}_x, \tilde{f}_y, \tilde{f}_z)$.

2.2. Calibration

Ideally, the force magnitude measured at the probe tip should not depend on the orientation of the force with respect to the probe. However, this is not always the case in practice, due to flexion in the probe structure that connects the force sensor to the contact point. Raw force data $\tilde{\mathbf{f}}^i = (\tilde{f}_x^i, \tilde{f}_y^i, \tilde{f}_z^i)$ collected at angle, i , spread 10° apart about a circle is displayed in Fig. 2. The \tilde{f}_z^i and \tilde{f}_{xy}^i display circular force data that has shifted from its expected position about the origin. In addition, \tilde{f}_z^i appears to be more off-center than \tilde{f}_{xy}^i . When a force is applied to the probe tip there is a small deflection of the probe shaft and the force sensor, relative to the rest of the plastic housing. Considering the geometry of the probe, when the probe shaft deflects, the axial force (\tilde{f}_z^i) moves in the direction of the force applied and the \tilde{f}_z^i increases. The larger shift in the axial force in contrast to

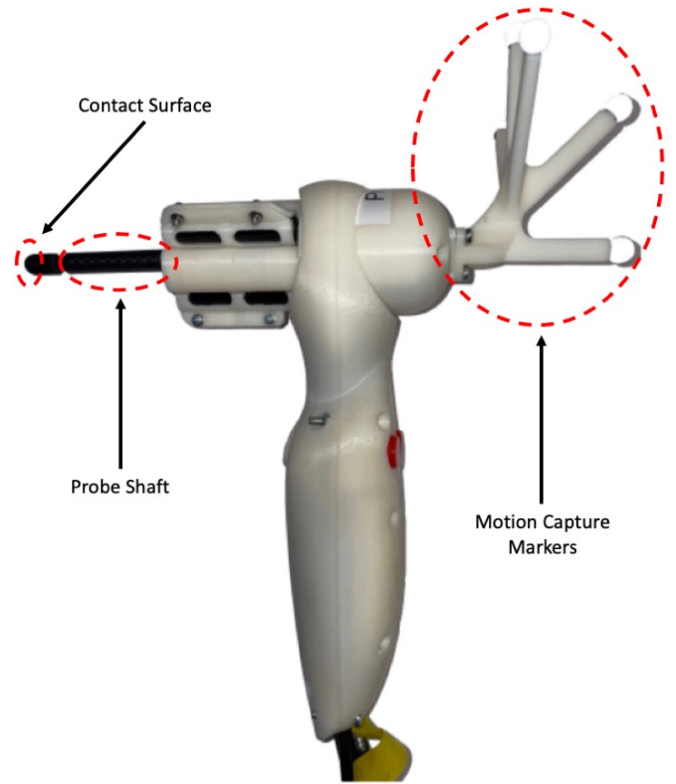


Figure 1: The handheld skin probe. The probe makes contact with a counter-surface at the probe tip's contact surface. Force data is collected from a force sensor housed within the probe and attached to the probe shaft. Motion capture markers track the position of the probe during measurements.

the radial force (\tilde{f}_{xy}) is potentially due to the larger distance between the force sensor and probe tip in the axial than radial direction. This asymmetry in the measurements motivates the calibration scheme. By systematically measuring the bias in the force data with a controlled calibration setup, the bias can be removed from any subsequent force measurement. The calibration process consists of three steps:

1. The probe is fixed in place, and the probe tip is pulled along 10° increments in all directions around the probe shaft. A force ratio (defined in Section 2.2.2) is calculated from the raw force data.
2. A unitless force ratio scale is computed for each measurement and used to fit a sinusoidal function, which closely approximates the data with a shifted circle.
3. The resulting scale function is used to remove the bias from subsequent force ratio measurements.

This calibration setup is advantageous for several reasons. First, by using a unitless scale factor, the calibration becomes magnitude independent. Second, by calibrating the force ratio, rather than individual forces, the exact force magnitude is not needed, and the calibration is robust with respect to parasitic frictional forces on the cord holding the calibration weight in the setup. Third, the calibration is applied to force ratios which are structurally similar and close to the Coulomb friction coefficient, making the results

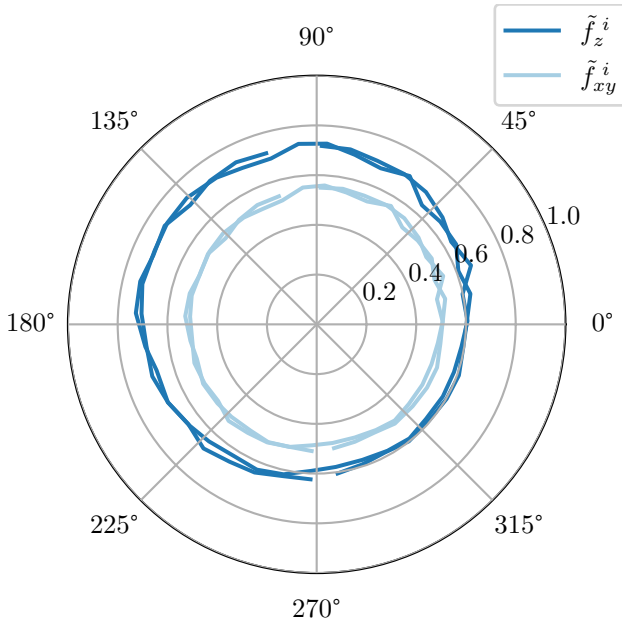


Figure 2: Raw force measurements measured at the probe tip during 2 complete circles of hanging a calibration weight 360° about a smoothly finished circle. An asymmetry of the force magnitude is observed for both \tilde{f}_{xy}^i and \tilde{f}_z^i , with a slightly larger bias in \tilde{f}_z^i

particularly suited for friction measurement. Finally, the calibration method is simple and repeatable. The method uses a smoothly finished wooden circle, a piece of inelastic string, and a calibration weight. These components are readily available through purchase, and typically already on hand at any laboratory.

The following two sections describe the calibration in more detail.

2.2.1. Force measurements

The calibration system measures a constant force applied 360° about the probe tip as shown in Fig. 3. The probe is clamped in place so that the probe tip is positioned vertically at the center of a smoothly finished wooden circle. A 100 g calibration weight is attached to the probe tip with a non-stretch cord so that the weight hangs off the edge of the circle. Raw force data $\tilde{\mathbf{f}}^i = (\tilde{f}_x^i, \tilde{f}_y^i, \tilde{f}_z^i)$ is collected at angle, i , spread 10° apart. The weight hangs for 1 minute at each location to allow it to settle.

Two complete circles of data collection define the calibration data. A third round of data is collected for validating the calibration. Before each circle of data collection, the wooden circle is rotated arbitrarily and recentered to reduce any bias due to systematic errors in the positioning of the setup.

2.2.2. Force ratio correction

Friction is defined in terms of the ratio between tangential and normal force components. This suggests that the calibration can be performed in force ratio space, which also tends to be less noisy than the total applied force (see

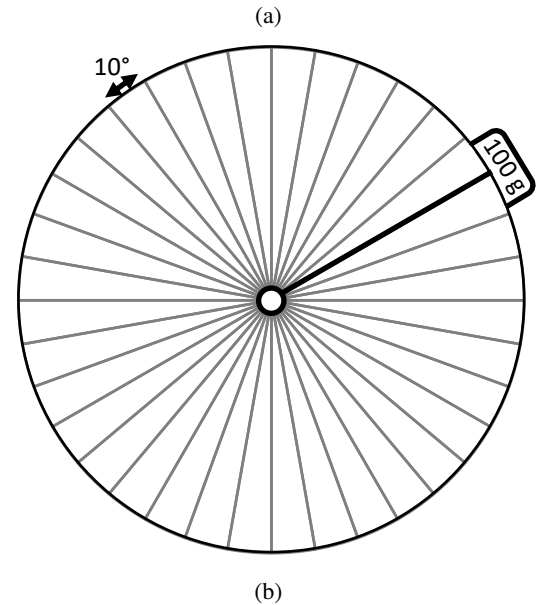
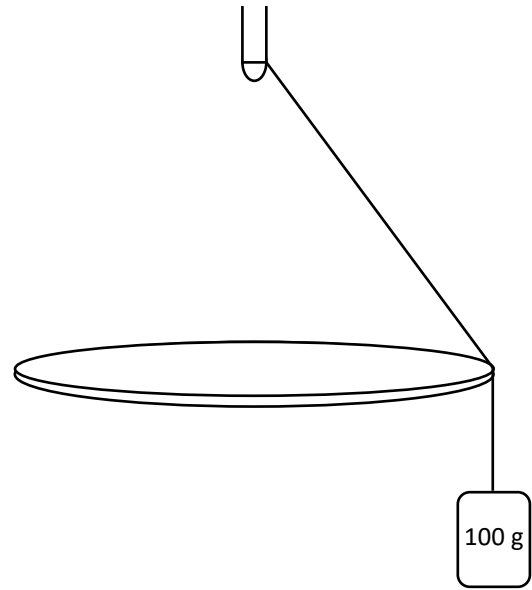


Figure 3: Circle calibration setup. The probe tip is positioned at the center of the circle and a 100 g calibration weight attached to the probe by a non-stretch cord is shifted 10° at a time to capture any bias in the force output.

Fig. 7a). Thus, at each i , a force ratio vector is calculated in terms of the raw calibration data as $\tilde{\mathbf{r}}^i = \tilde{\mathbf{f}}_{xy}^i / \tilde{f}_z^i$ where $\tilde{\mathbf{f}}_{xy}^i = (\tilde{f}_x^i, \tilde{f}_y^i)$ is the tangential force.

To make the result of the calibration scale independent, it is performed on a unitless scale factor rather than the force ratio directly. For each i , a scale factor, γ^i , is calculated by which to scale our measured force ratio $\tilde{\mathbf{r}}^i$ such that $\|\tilde{\mathbf{r}}^i\| \gamma^i = \rho$, where ρ is the average force ratio defined as

$$\rho = \frac{1}{n} \sum_{i=1}^n \|\tilde{\mathbf{r}}^i\|. \quad (1)$$

Here n is the total number of measurements around one circle ($n = 36$). The bias in γ^i closely follows a simple sinusoidal pattern periodic with angle θ . This suggests that the error in force ratio measurements can be corrected by a continuous sinusoidal function for any angle θ . Thus, the scale factors γ^i are fit to a generalized sine function

$$\Gamma(\theta; A, \phi, \beta) = A \sin(\theta + \phi) + \beta \quad (2)$$

where A , ϕ and β are the fitting parameters. Formally, the following non-linear least squares problem is solved

$$(\bar{A}, \bar{\phi}, \bar{\beta}) = \arg \min_{A, \phi, \beta} \frac{1}{2} \sqrt{\sum_{i=1}^n (\Gamma(\theta^i; A, \phi, \beta) - \gamma^i)^2} \quad (3)$$

where $\theta^i = \arctan(\tilde{f}_y^i / \tilde{f}_x^i)$. Equation (3) is solved using Levenberg–Marquardt with the `lmfit` Python package [26]. Due to the regularity in the samples γ^i , it may suffice to use far fewer than 36 samples, but at least 3 is required to find a unique solution to (3).

After calibration, $\Gamma(\cdot; \bar{A}, \bar{\phi}, \bar{\beta})$ can be used to correct any measured force ratio $\tilde{\mathbf{r}} = \tilde{\mathbf{f}}_{xy} / \tilde{f}_z$ as follows

$$\mathbf{r} = \tilde{\mathbf{r}} \Gamma(\arctan(\tilde{f}_y, \tilde{f}_x); \bar{A}, \bar{\phi}, \bar{\beta}) \quad (4)$$

Results showed a larger variability in \tilde{f}_z than $\tilde{\mathbf{f}}_{xy}$ as seen in Fig. 2, indicating that the flexion bias has the largest affect on \tilde{f}_z . Therefore, \tilde{f}_z is adjusted rather than $\tilde{\mathbf{f}}_{xy}$. The calibrated force along the z-axis is found with

$$f_z = \|\tilde{\mathbf{f}}_{xy}\| / \|\mathbf{r}\| \quad (5)$$

while keeping the in-plane force unchanged $f_{xy} = \tilde{\mathbf{f}}_{xy}$. Hereafter we refer to the calibrated force frame at the probe tip as $\mathbf{f} = (f_x, f_y, f_z)$.

2.3. Surface correction

A sliding tribometer applied to an irregular curved surface like human skin, cannot be kept reliably perpendicular to the contact surface without a strictly controlled environment. This problem is further exacerbated when the tribometer is handheld. Fig. 4 depicts 2D examples where the tribometer’s measured force frame (f_x and f_z) is aligned and misaligned with the contact force frame (f_N and f_T) at the contact point between the tip of a tribometer and the measured surface. It would be an error to assume that $f_N = f_z$ and $f_T = f_x$ on the downward curve in Fig. 4.

In theory, it is possible to correct for this misalignment if the shape, position, and rotation of the two contacting surfaces is known. It is also assumed that the transformation from the probe-tip frame to the tribometer’s force sensor frame is known. With this information the shapes of the measurement target and tribometer contact surface can be registered to their respective locations and the contact point between the two surfaces can be calculated (see Section 3.2 for a discussion of tools available for 3D scanning and surface registration). Fig. 5 shows a 2D representation of the

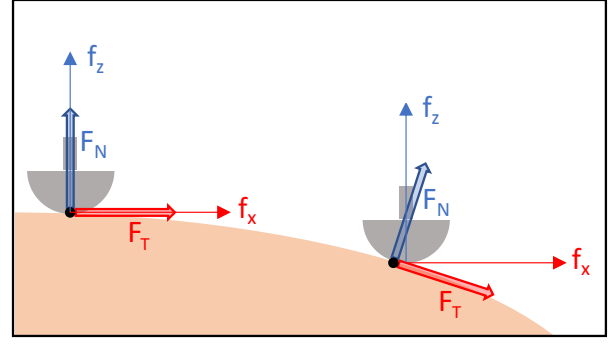


Figure 4: Force frame alignment. When a tribometer is positioned perpendicular to a flat surface, the f_x and f_z measured at the tribometer’s force frame are aligned with f_N and f_T at the surface contact frame. As the tribometer moves across a curved surface, the frames rotate out of alignment, and the location of the contact point on the probe tip changes

surface of a tribometer and the surface of a measurement target in contact, where $\hat{\mathbf{t}}$ is the tribometer shaft frame’s orientation (aligned with force sensor’s “z” direction) and $\hat{\mathbf{n}}$ is the contact normal (aligned with the contact frame’s “z” direction). The transformation from the tribometer measurements to measurements in the contact frame simplifies to a pure rotation if we assume the tip is spherical (as it is, in our device), and the radius is small relative to the length of the probe shaft. While spherical probes are ubiquitous in linear tribometers [1, 14, 30, 3], it is possible to generalize this analysis with affine transformations for the case of more general probe tip shapes.

Let \mathbf{R} be a rotation matrix such that

$$\mathbf{R}\hat{\mathbf{t}} = \hat{\mathbf{n}} \quad (6)$$

Then the forces measured in the tribometer’s frame can be transformed to the contact point frame via a change of basis matrix, which in this case is $\mathbf{R}^{-1} = \mathbf{R}^T$:

$$\mathbf{f}^{\text{adj}} = \mathbf{R}^{-1} \mathbf{f} \quad (7)$$

where \mathbf{f}^{adj} is the adjusted force frame at the contact surface. If the position and rotation of the two contacting surfaces is being recorded continuously during a sliding contact, then it is possible to estimate the forces in the contact point frame across a surface with curved geometry. For force ratios, the same change of basis can be applied to $(\mathbf{r}, 1) \in \mathbb{R}^2 \times \mathbb{R}$ to generate the adjusted force ratio

$$\mathbf{r}^{\text{adj}} = \mathbf{R}^{-1} \begin{pmatrix} \mathbf{r} \\ 1 \end{pmatrix}. \quad (8)$$

The next two sections describe the implementation of this surface correction in a controlled measurement environment.

2.4. Measurement

To test the surface correction, an experiment was designed to measure friction on various curved surfaces. A

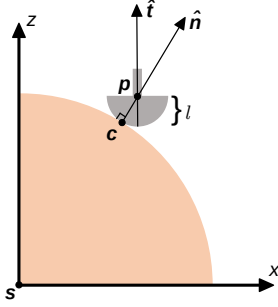


Figure 5: Surface correction diagram. A probe tip with orientation \hat{t} touches the cylinder centered on s at the point c . The center of the probe is located at p , which conveniently determines the normal \hat{n} due to the geometry of the probe and cylinder.

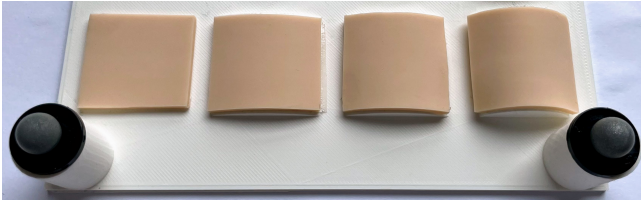


Figure 6: Friction measurement target.

measurement target (Fig. 6) was designed and 3D printed (Ultimaker 3, Netherlands) to systematically vary the curvature of the surface that the probe tip travels along. The target consists of four 3x3 cm measurement areas with varied curvature: flat and sections of cylinders with radii of 4.5 cm, 3 cm, and 1.5 cm. A skin-like silicone sheet was securely attached to each measurement area. Motion capture markers were attached to raised posts to track the position of the measurement target.

The axes of the cylindrical target surfaces were aligned along the y -axis of the motion capture coordinate world frame. This way the surface correction can be performed entirely in the xz -plane.

The probe tip and target surface were cleaned with an isopropyl alcohol solution and allowed to dry for 20 minutes before measurements were collected. 5 reciprocating cycles of sliding data were collected for each measurement area. To ensure the angle of the probe relative to the curved surfaces varied over time, the probe was held vertically for all trials across each surface. The experimenter moved the probe so that the path traveled during sliding followed the x -axis (\tilde{f}_x) of the probe tip force frame. The correction applied here is in 2D, therefore, it was important to minimize the measured \tilde{f}_y , as it was not corrected in this example.

2.5. Surface correction example

To estimate f_N and f_T the general surface correction strategy from Section 2.3 is applied to the measurement data collected in Section 2.4.

The target's surface shape is known from the 3D print design and the position of the surface shape was registered

to the motion capture markers. Let $\mathbf{p} = (p_x, p_y, p_z)$ be the center point of the spherical probe tip (see Fig. 5) in world coordinates and $\mathbf{s} = (s_x, s_y, s_z)$ be the position of the center of each cylinder aligned with the probe tip on the y -axis. Due to the cylindrical geometry of the contact surface and the spherical geometry of the probe tip, the contact unit normal can be computed simply as

$$\hat{n} = \frac{\mathbf{p} - \mathbf{s}}{\|\mathbf{p} - \mathbf{s}\|} \quad (9)$$

The contact point can then be computed as $\mathbf{c} = \mathbf{p} - l\hat{n}$, where l is the radius of the probe tip.

In general, \hat{t} is determined from the tracked motion capture markers attached to the skin probe. In the experimental setup, it is close to $(0,0,1)$, since the experimenter holds the probe vertically. With the known values of \hat{n} and \hat{t} the rotation matrix R can be computed according to Eq. (6) using Rodrigues' formula:

$$R = I + \sin \alpha [\hat{\mathbf{k}}]_{\times} + (1 - \cos \alpha) [\hat{\mathbf{k}}]_{\times}^2$$

where $\cos \alpha = \hat{t} \cdot \hat{n}$, I is the 3x3 identity, $\hat{\mathbf{k}} = \hat{t} \times \hat{n} / \|\hat{t} \times \hat{n}\|$ and $[\cdot]_{\times}$ is the cross product matrix:

$$[\mathbf{k}]_{\times} = \begin{bmatrix} 0 & -k_z & k_y \\ k_z & 0 & -k_x \\ -k_y & k_x & 0 \end{bmatrix}.$$

By definition f_z is aligned with \hat{t} and therefore f_x is orthogonal to \hat{t} . Each force measurement at the probe tip frame was transformed to the contact frame with Eq. (7), where $\mathbf{f} = (f_x, f_y, f_z)$ and $\mathbf{f}^{\text{adj}} = (f_x^{\text{adj}}, f_y^{\text{adj}}, f_z^{\text{adj}})$.

The normal and tangential forces at the contact point are defined via

$$\begin{aligned} f_N &= f_z^{\text{adj}} \\ f_T &= \|(f_x^{\text{adj}}, f_y^{\text{adj}})\|. \end{aligned}$$

Note that $f_y^{\text{adj}} = f_y$ here since the cylinder is aligned with the y -axis, thereby there is no curvature to correct for in the y direction.

To compare results of the calibrated forces and the corrected forces, the calibrated force ratio is defined as $r = f_{xy}/f_z$ where $f_{xy} = \|(f_x, f_y)\|$ and the corrected force ratio is then given by $r_c = f_T/f_N$. Equivalently the corrected ratio can be computed directly using Eq. (8) as $r_c = \|(r_x^{\text{adj}}, r_y^{\text{adj}})\|/r_z^{\text{adj}}$, where $\mathbf{r}^{\text{adj}} = (r_x^{\text{adj}}, r_y^{\text{adj}}, r_z^{\text{adj}})$.

3. Results and Discussion

3.1. Calibration

Fig. 7a shows the measured \tilde{f}_{xy}^i , \tilde{f}_z^i , $\tilde{\mathbf{r}}^i$, and \mathbf{r} from the two circles of calibration data collected. The varied starting locations of the hanging calibration weight can be identified by the gaps in the polar plot. A larger variance in \tilde{f}_z^i than \tilde{f}_{xy}^i is observed as the calibration weight is moved about the circle. The calibration data produces $\rho = 0.79$ from Eq. (1).

Fig. 7a shows how applying the calibration directly to $\tilde{\mathbf{r}}^i$ produces a close approximation \mathbf{r} to the circle with radius ρ centered at the origin as expected. This demonstrates that the calibration is working correctly. Fig. 7b shows the validation trial for the calibration. A similar asymmetry is observed in $\tilde{\mathbf{r}}^i$, but after calibration, \mathbf{r} is well centered around the origin.

To demonstrate the impact this calibration makes on sliding force data collected with the skin probe, Fig. 8 shows $\tilde{\mathbf{r}}^i$ and \mathbf{r} from reciprocal sliding along a flat silicone surface. An asymmetry in $\tilde{\mathbf{r}}^i$ is observed in the raw experimental data, where sliding in one direction produces a larger force ratio than sliding in the opposite direction. After the calibration is applied a similar \mathbf{r} is produced regardless of sliding direction.

The value of ρ can be changed in this calibration setup by increasing or decreasing the angle between the non-stretch cord and the smoothly finished wooden disc. Here, $\rho = 0.79$ is chosen because it is within the range of force ratios collected during the sliding experiment. The asymmetry seen in \tilde{f}_z^i and \tilde{f}_{xy}^i may be due to flexion in the plastic that the probe is built from. This flexion is likely not isotropic and changes non-linearly when the force applied is varied. A useful future direction for this type of calibration would be to collect calibration data at various angles to represent a large range of values of ρ .

3D printers and related technology have become ubiquitous across research centers. These machines are extremely useful, as they allow researchers to build tools for specific applications that would not exist otherwise. Nevertheless, this opens the door to errors if researchers are not meticulous about construction and data validation. To ensure that the data produced by these tools is accurate and precise, it is imperative to be critical of the design and test it stringently. Here, a direction-dependent inconsistency in the force output may be unavoidable, however, this type of error can be systematically identified and corrected. Otherwise, it likely would lead to attributing the bias seen in the data to the real properties of the surfaces that are being measured.

3.2. Surface Correction

Sliding contact data between the probe tip surface and the measurement target was collected. Fig. 9 displays data from a single sliding trial across the friction target curve with a 3 cm radius. At the beginning of the measurement the probe tip moves up the curve where f_{xy} and f_z reach their maximum and minimum values respectively due to the contact's minimum angle between the probe's leading edge and the surface of the curve. The reverse trend for f_{xy} and f_z is observed as the probe begins to descend along the curve at the end of the contact.

After the surface correction is applied to f_{xy} and f_z in Fig. 9, the variability in f_{xy} and f_z is decreased in the calculated f_T and f_N . For such a sliding contact, when the f_N increases, the f_T is expected to increase, and when the f_N decreases, the f_T is also expected to decrease. Here, the f_T and f_N are both increasing over time, whereas the f_{xy} and f_z are trending in opposite directions. The probe tip

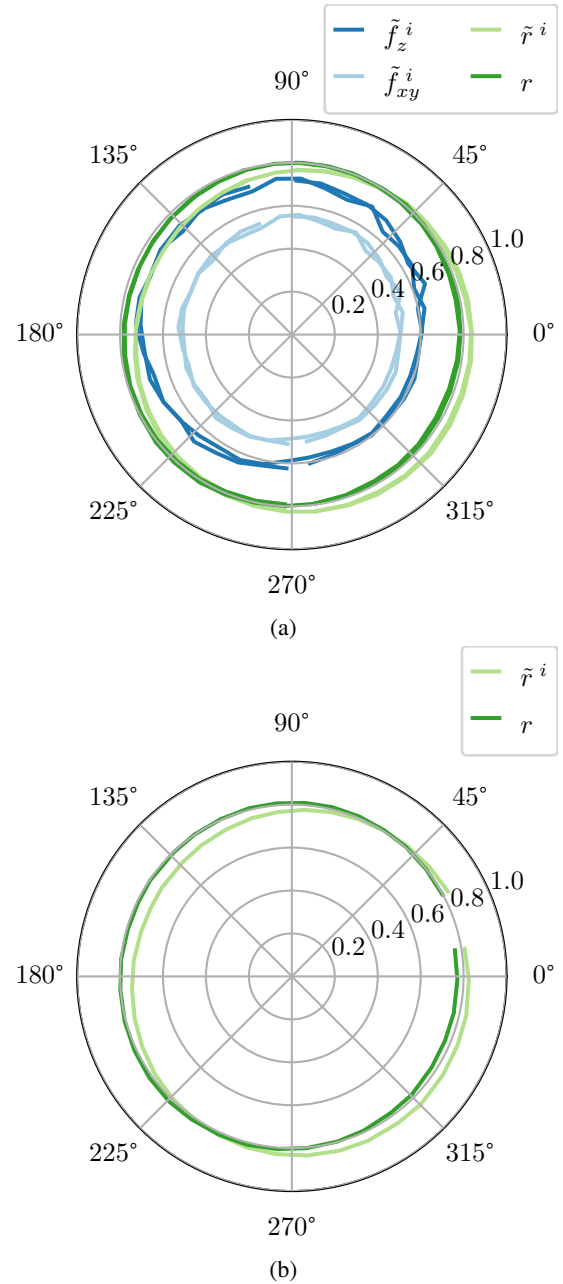


Figure 7: Probe force calibration. Fig. 7a displays the measured normal and tangent force of each measurement around the circle and the calculated force ratio before and after calibration is applied. Fig. 7b shows a validation trial, where the calibration calculated in Fig. 7a is used to correct the force ratio of a separate collection of force measurements about the circle

forces (f_{xy} and f_z) and contact surface forces (f_T and f_N) intersect at the apex of the measurement target curve where the probe tip coordinate frame is equal to the contact point coordinate frame (i.e. $\hat{\mathbf{i}} = \hat{\mathbf{n}}$).

When working with a force sensor, an elastic element, it is important to consider if the effective bandwidth of the tribometer is affecting the force data [37]. It is noted that even though the resonant frequency of the force sensor is rated by the manufacturer as 7200 Hz, the effective bandwidth

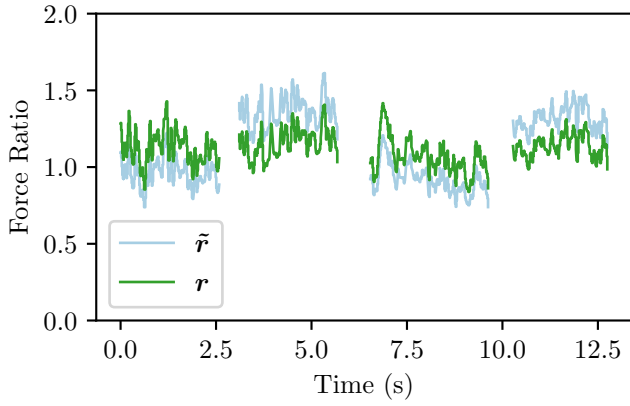


Figure 8: Force ratio data from reciprocal sliding along a flat silicone surface before and after the calibration has been applied. The change of sliding direction can be identified by the break in the data.

of the sensor system (including the stiff carbon fiber probe shaft) could be significantly lower (a back of the envelope estimate suggests 10-100Hz). However, this work does not attempt to characterize the specific modes of the system. A spectral analysis suggests the dominant oscillations seen in the force data are in the 1-3 Hz range. These oscillations are hypothesized to be due to a combination of stick-slip between the surfaces and physiological tremor from the experimenter.

Fig. 10 shows r and r_c of single touches across the four measurement target curve conditions. The correction in the flat surface condition, shown in Fig. 10a, demonstrates that it is necessary to account for the orientation of the probe even in ideal conditions. Regardless of the experimenter's attempt to hold the probe 90° to the flat target surface, there still existed a bias to hold the probe at a slight angle, which resulted in $r > r_c$. This is an important result to consider when using handheld linear sliding tribometers. Even if the measurement area is flat, there is still a high probability that the tribometer is not perpendicular to the surface. In addition, even when using robotic tribometers it is essential that the measurement area is correctly aligned on the sampling platform.

Regarding the curved surfaces (Fig. 10b, Fig. 10c, and Fig. 10d), the r displays a negative slope as the probe tip moves across all three of the curves. This trend is expected, as the data in Fig. 9 shows an increasing f_z and a decreasing f_{xy} . The magnitude of the negative slope and the variability of r increase as the radius of the measurement curves decreases (i.e. slope of the curve increases). The r in Fig. 10d has a maximum value above 3 and a minimum value close to 0.

Applying the surface correction produces two improvements in the curved surface contact data. First, the negative slope and large within-condition variability of r are replaced with flatter and more consistent r_c . Second, there is more consistency in r_c between-conditions. These observations

Curve	Data	Force ratio			
		mean	std	min	max
1.5	r_c	1.09	0.24	0.10	2.68
	r	5.66	42.04	0.00	1435.49
3.0	r_c	0.90	0.12	0.54	1.27
	r	1.13	0.63	0.18	5.45
4.5	r_c	0.93	0.13	0.55	1.42
	r	1.01	0.46	0.32	3.30
flat	r_c	1.05	0.18	0.62	1.66
	r	1.07	0.22	0.57	1.76

Table 1
Summary statistics for Fig. 11

are promising, given that the probe tip surface and the silicone surface are constant across conditions this consistency indicates that the surface correction is working as expected.

Fig. 11 shows force ratio data for all sliding trials across all surface conditions. Table 1 summarizes the statistics for Fig. 11. The trends shown in Fig. 10 are visible in this overview of the data set. There is an overall larger variance in r than in r_c , and this variance increases as the radius of the curves decreases. The difference between r and r_c on the flat surface is minimal. The medians of r and r_c are similar for each curve and across conditions. This can be explained by acknowledging that the curves are symmetric, therefore, the same location on the opposite side of each curve will give an inverse force result and a median close to the r and r_c at the apex of the curve where the r approaches r_c due to the probe shaft being close to perpendicular to the curve surface. If the curves were not symmetric there would be larger differences in medians.

It is acknowledged that the highly controlled experimental setup and confining the surface correction to 2D has not truly tested the limits of this methodology. However, this work should motivate future work to expand the correction methods to 3D and measure on more complex shapes, such as a human body. Adding an extra dimension to the analysis will bring challenges, such as registering the surface topography of the measurement surfaces to the motion capture data. An extra dimension introduces an opportunity for a larger error. As well, registering a surface mesh of a non-rigid surface (such as a human body) is a difficult problem to solve and is exacerbated if the human is in different poses during the scan and motion capture; even subtle pose changes such as shoulder slouching. Another challenge will be estimating the vector normal at the contact point. There exists useful open-source geometry processing libraries (e.g. libigl) to assist with estimating the normal, however, these results will rely on the quality of the surface mesh constructed from the raw data of a 3D scanner or some other means.

The principles of the method remain the same and with 3D scanning technology rapidly improving and becoming more available, researchers will be able to gather reliable 3D data for this type of correction. Full-body 3D scanners

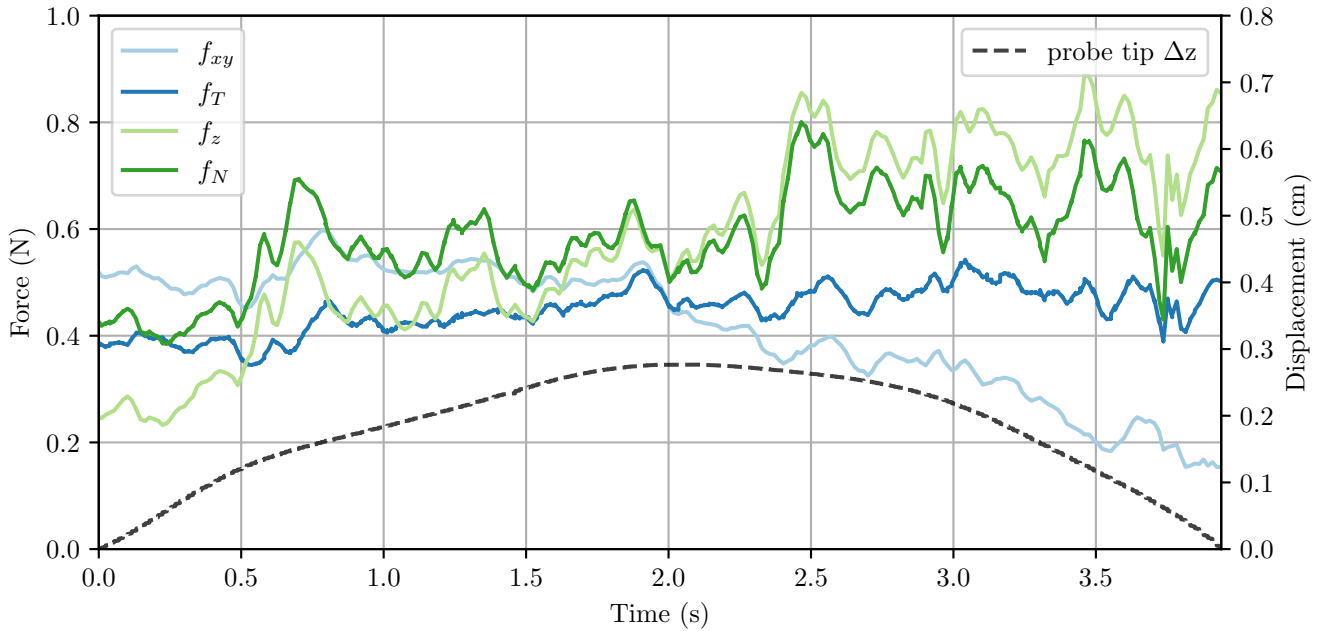


Figure 9: Raw and surface corrected forces of one slide across a curved surface on the measurement target. The probe tip's height as it moves across the curve is plotted along the same time sequence.

(e.g. VITUS 3D Body Scanner, Vitronic, Germany) are excellent tools, but are expensive and require a large space to store them. Less monetary and space expensive methods exist for 3D mesh construction, such as photogrammetry. Photogrammetry is a process to extract 3D information from a set of overlapping photographic data. Software is available to researchers, either open-source (e.g. Meshroom) or commercial (e.g. Agisoft), where the user only needs to supply a set of photographs collected with a smartphone camera at minimum.

A 3D mesh may even be constructed with a motion capture system. If the probe tip is traced over the measurement area, then that position data may be used to reconstruct a 3D surface mesh. Figure 12 shows \mathbf{p} plotted over the shape of a curve on the measurement target. Quantification of the difference between the two curves shows a difference in area of 0.57 mm^2 and a discrete Fréchet distance of 0.68 mm [18]. This suggests a good estimation of the shape of the target, however, the deformation of a soft surface during this hypothetical “probe scanning” can be problematic. The probe paths would vary depending on the normal force used and may lead to an irregular surface mesh. As well, in a research setting with human participants, it is important to consider the time that they are in the lab. Full-body 3D scanners can produce a high-quality 3D mesh in 10 seconds. It may take some time to collect and quality check the data from the “probe scanning”. Nevertheless, this may be an interesting option to explore instead of the 3D scanner if it is not easily accessible.

Accurately tracking the motion of the measurement target and the tribometer may prove to be more difficult without a motion capture system. This work relies on a Vicon Motion Capture system and, similar to the full-body 3D scanner, this

tool produces excellent data but it is expensive and requires space to store. A less expensive and promising future direction is markerless motion capture; there have recently been significant advances in this field (e.g. OpenPose). This technology does not rely on the sensors that attach to the human body for classic motion capture but instead just requires a set of standard video cameras. With photogrammetry and markerless motion capture, it may be possible to collect all the necessary data with a set of smartphone cameras in the near future.

A final consideration is that the surface topography is only one factor of many that is important to consider when measuring friction on soft surfaces. One of these important considerations for the probe is the surface material at the probe tip contact area. In this paper, the probe tip is 3D printed with polylactic acid, however, the probe tip can be exchanged for tips of different shapes and materials. Friction measurements depend on other surfaces and this will need to be considered when exchanging probe tips. Other considerations for measuring friction include fluids and moisture between the two surfaces. This is outside the scope for this research article, but should be considered when measuring friction with human skin. Tools such as the Corneometer@CM 825 and Sebumeter@SM 815 (Courage & Khazaka Electronics, Germany) can measure moisture and surface oils on the skin, respectively. This information can compliment the data collected from the skin probe.

4. Conclusion

In this paper, a new method is proposed for estimating normal and tangential forces on curved surfaces using a handheld tribometer. The method is tested by measuring forces during sliding contacts on curved surfaces. The

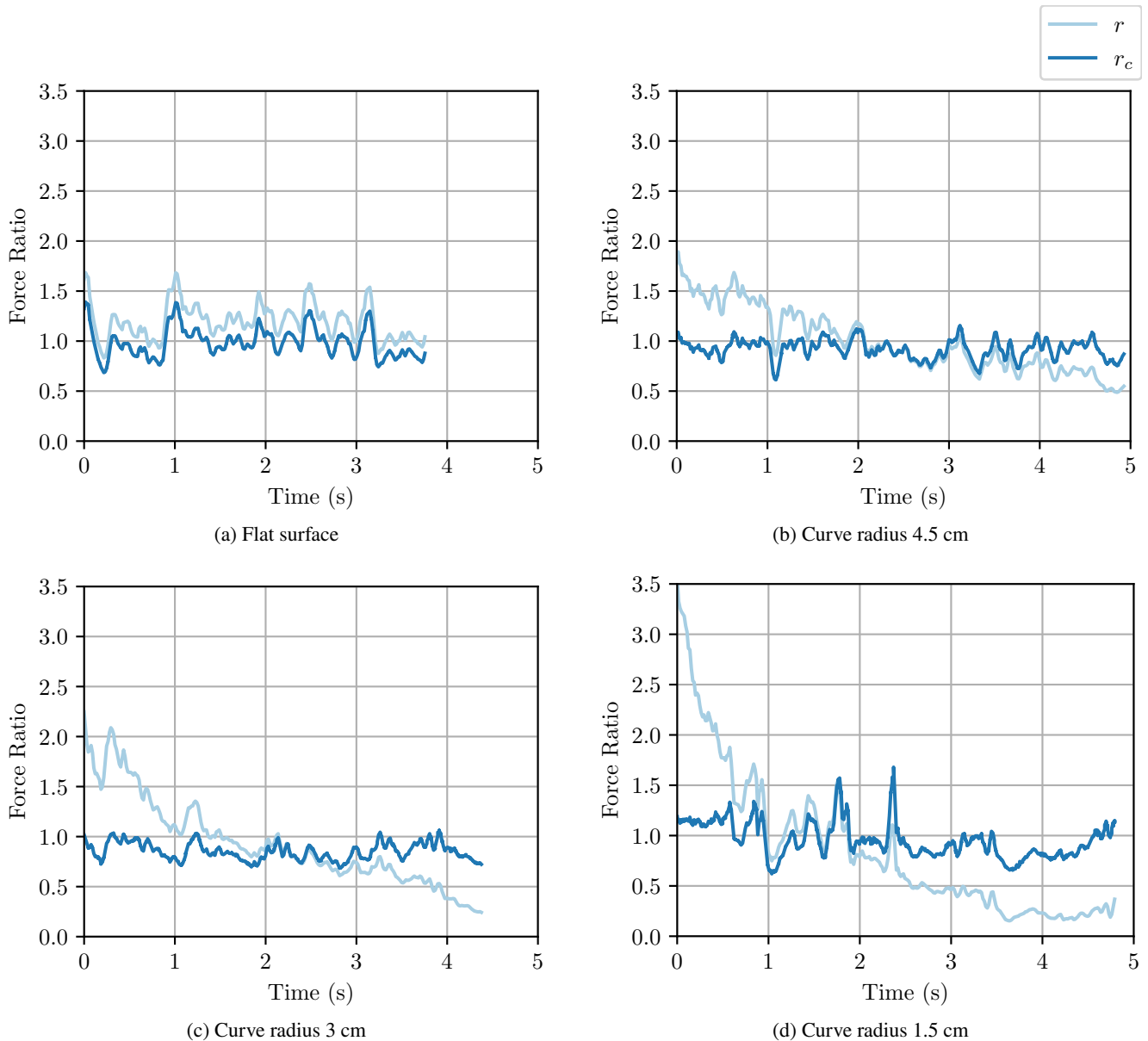


Figure 10: Calibrated force ratios (r) and corrected force ratios (r_c) of single slides across four surface curve conditions of the measurement target

curved surface adjustment significantly improved the estimation of forces and produced a more consistent force ratio. In addition, a simple but careful procedure is described for calibrating a friction measurement instrument, custom-made with 3D printing techniques that are becoming more widely available. This technique demonstrates a way to measure intrinsic bias within such devices and effectively correct for said bias to improve the accuracy of measurement data.

Funding Sources

This work was supported, in part, by NSERC Discovery (GR010268), NSERC RTI (GRO19523), and the Canada Foundation for Innovation (LEF20419) grants.

References

- [1] Adams, M.J., Briscoe, B.J., Johnson, S.A., 2007. Friction and lubrication of human skin. *Tribology Letters* 26, 239–253. URL: <http://link.springer.com/10.1007/s11249-007-9206-0>, doi:10.1007/s11249-007-9206-0.
- [2] Akers, W.A., 1985. Measurements of friction injuries in man. *American Journal of Industrial Medicine* 8, 473–481. URL: <http://doi.wiley.com/10.1002/ajim.4700080429>, doi:10.1002/ajim.4700080429.
- [3] Asserin, J., Zahouani, H., Humbert, P., Couturaud, V., Mouglin, D., 2000. Measurement of the friction coefficient of the human skin in vivo: Quantification of the cutaneous smoothness. *Colloids and Surfaces B: Biointerfaces* 19, 1–12. doi:10.1016/S0927-7765(99)00169-1.
- [4] Bertaux, E., Lewandowski, M., 2007. Relationship between friction and tactile properties for woven and knitted fabrics. *Textile Research Journal* 77, 387–396. URL: www.trj.sagepub.com<http://trj.sagepub.com>, doi:10.1177/0040517507074165.

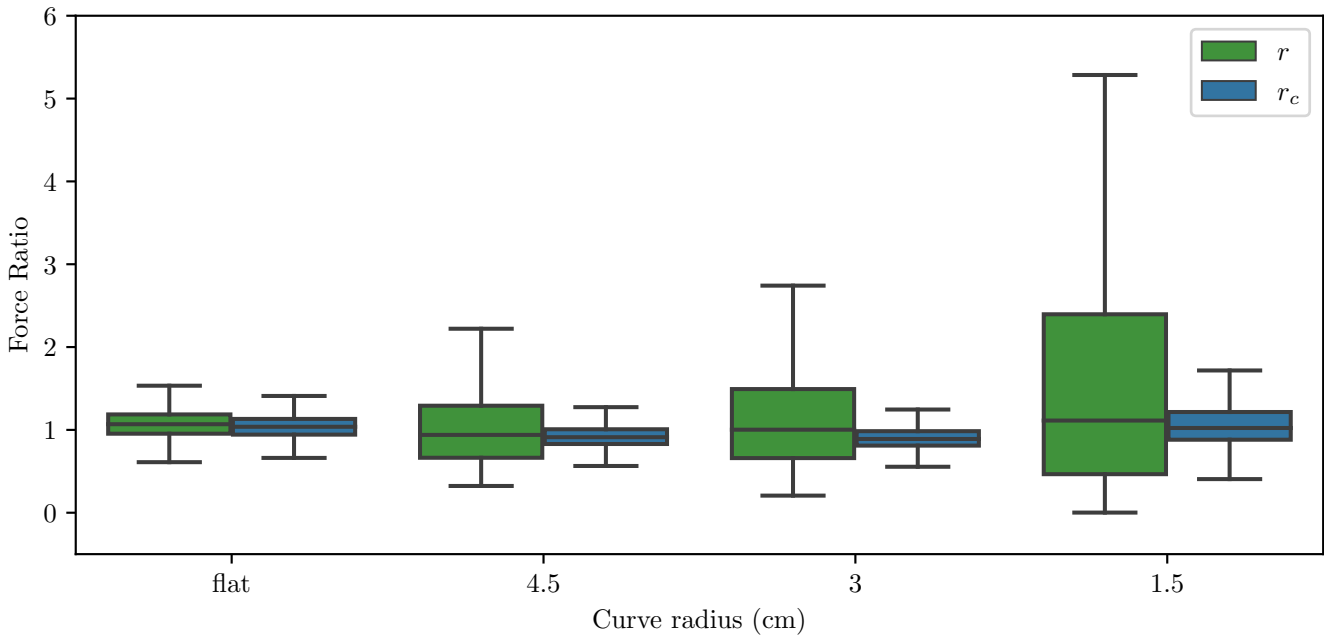


Figure 11: All r and r_c data points were collected from all trials moving across the curvature conditions of the measurement target.

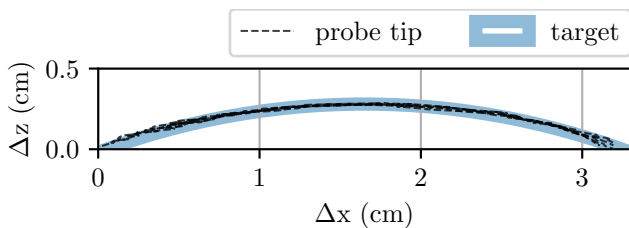


Figure 12: Position of the probe tip (p) from multiple slides on the measurement target plotted over the shape of the corresponding curve.

[5] Cua, A.B., Wilhelm, K.P., Maibach, H.I., 1990. Frictional properties of human skin: relation to age, sex and anatomical region, stratum corneum hydration and transepidermal water loss. *British Journal of Dermatology* 123, 473–479. URL: <http://doi.wiley.com/10.1111/j.1365-2133.1990.tb01452.x>, doi:10.1111/j.1365-2133.1990.tb01452.x.

[6] Cua, A.B., Wilhelm, K.P., Maibach, H.I., 1995. Skin surface lipid and skin friction: relation to age, sex and anatomical region. *Skin Pharmacology and Physiology* 8, 246–251. URL: <https://www.karger.com/Article/FullText/211354>, doi:10.1159/000211354.

[7] Derler, S., Gerhardt, L.C., 2012. Tribology of skin: review and analysis of experimental results for the friction coefficient of human skin. *Tribology Letters* 45, 1–27. URL: <http://link.springer.com/10.1007/s11249-011-9854-y>, doi:10.1007/s11249-011-9854-y.

[8] Derler, S., Schrade, U., Gerhardt, L.C., 2007. Tribology of human skin and mechanical skin equivalents in contact with textiles. *Wear* 263, 1112–1116. URL: https://ac.els-cdn.com/S0043164807003535/1-s2.0-S0043164807003535-main.pdf?_tid=3ce5a3d4-8b8a-4a37-ade8-4093a90a79d0&acdnat=1537546692_2e55fbdf33c5d59b8b929b507d64ce6e, doi:10.1016/j.wear.2006.11.031.

[9] Dong, Y., Kong, J., Mu, C., Zhao, C., Thomas, N.L., Lu, X., 2015. Materials design towards sport textiles with low-friction and moisture-wicking dual functions. *Materials & Design* 88, 82–87. URL: <https://www.sciencedirect.com/science/article/pii/S0264127515303567>, doi:10.1016/J.MATDES.2015.08.107.

[10] Eisner, P., Wilhelm, D., Maibach, H.I., 1990. Frictional properties of human forearm and vulvar skin: influence of age and correlation with transepidermal water loss and capacitance. *Dermatology* 181, 88–91. URL: <https://www.karger.com/Article/FullText/247892>, doi:10.1159/000247892.

[11] Essick, G.K., McGlone, F., Dancer, C., Fabricant, D., Ragin, Y., Phillips, N., Jones, T., Guest, S., 2010. Quantitative assessment of pleasant touch. *Neuroscience and Biobehavioral Reviews* 34, 192–203. doi:10.1016/j.neubiorev.2009.02.003.

[12] Gee, M.G., Tomlins, P., Calver, A., Darling, R.H., Rides, M., 2005. A new friction measurement system for the frictional component of touch. *Wear* 259, 1437–1442. doi:10.1016/j.wear.2005.02.053.

[13] Gerhardt, L.C., Strässle, V., Lenz, A., Spencer, N.D., Derler, S., 2008. Influence of epidermal hydration on the friction of human skin against textiles. *Journal of the Royal Society, Interface* 5, 1317–1328. URL: <http://www.ncbi.nlm.nih.gov/pubmed/18331977http://www.pubmedcentral.nih.gov/articlerender.fcgi?artid=PMC2607440>, doi:10.1098/rsif.2008.0034.

[14] Gitis, N., Sivamani, R., 2004. Tribometry of skin. *Tribology Transactions* 47, 461–469. doi:10.1080/05698190490493355.

[15] Gwosdow, A.R., Stevens, J.C., Berglund, L.G., Stolwijk, J.A.J., 1986. Skin friction and fabric sensations in neutral and warm environments. *Textile Research Journal* 56, 574–580. URL: <http://journals.sagepub.com/doi/10.1177/004051758605600909>, doi:10.1177/004051758605600909.

[16] Hendriks, C.P., Franklin, S.E., 2010. Influence of surface roughness, material and climate conditions on the friction of human skin. *Tribology Letters* 37, 361–373. URL: <http://link.springer.com/10.1007/s11249-009-9530-7>, doi:10.1007/s11249-009-9530-7.

[17] Janko, M., Wiertelwski, M., Visell, Y., 2018. Contact geometry and mechanics predict friction forces during tactile surface exploration. *Scientific Reports* 8, 1–10. URL: <http://www.nature.com/articles/s41598-018-23150-7>, doi:10.1038/s41598-018-23150-7.

[18] Jekel, C.F., Venter, G., Venter, M.P., Stander, N., Haftka, R.T., 2019. Similarity measures for identifying material parameters from hysteresis loops using inverse analysis. *International Journal of Material Forming* 12, 355–378. URL: <https://link.springer.com/article/10.1007/s12289-018-1421-8>, doi:10.1007/s12289-018-1421-8/FIGURES/29.

[19] Johnson, S.A., Gorman, D.M., Adams, M.J., Briscoe, B.J., 1993. The friction and lubrication of human stratum corneum. *Tribology Series*

- 25, 663–672. URL: <https://www.sciencedirect.com/science/article/abs/pii/S016789220870419X>, doi:10.1016/S0167-8922(08)70419-X.
- [20] Klöcker, A., Wiertelowski, M., Théate, V., Hayward, V., Thonnard, J.L., 2013. Physical factors influencing pleasant touch during tactile exploration. *PLoS ONE* 8, e79085. URL: <http://dx.plos.org/10.1371/journal.pone.0079085>, doi:10.1371/journal.pone.0079085.
- [21] Koudine, A.A., Barquins, M., Anthoine, P.H., Aubert, L., Leveque, J.L., 2000. Frictional properties of skin: proposal of a new approach. *International Journal of Cosmetic Science* 22, 11–20. URL: <http://doi.wiley.com/10.1046/j.1467-2494.2000.00006.x>, doi:10.1046/j.1467-2494.2000.00006.x.
- [22] Larionov, E., Fan, Y., Pai, D.K., 2021. Frictional contact on smooth elastic solids. *ACM Transactions on Graphics (TOG)* 40, 1–17. URL: <https://dl.acm.org/doi/abs/10.1145/3446663>, doi:10.1145/3446663.
- [23] Li, J., Daviet, G., Narain, R., Bertails-Descoubes, F., Overby, M., Brown, G.E., Boissieux, L., 2018. An implicit frictional contact solver for adaptive cloth simulation. *ACM Transactions on Graphics (TOG)* 37, 1–15. URL: <https://dl.acm.org/doi/abs/10.1145/3197517.3201308>, doi:10.1145/3197517.3201308.
- [24] Li, W., Kong, M., Liu, X., Zhou, Z., 2008. Tribological behavior of scar skin and prosthetic skin in vivo. *Tribology International* 41, 640–647. URL: <https://www.sciencedirect.com/science/article/pii/S0301679X07001934>, doi:10.1016/J.TRIBOINT.2007.11.009.
- [25] Naylor, P.F.D., 1955. The skin surface and friction. *British Journal of Dermatology* 67, 239–248. URL: <http://doi.wiley.com/10.1111/j.1365-2133.1955.tb12729.x>, doi:10.1111/j.1365-2133.1955.tb12729.x.
- [26] Newville, M., Stensitzki, T., Allen, D.B., Ingargiola, A., 2014. LMFIT: non-linear least-square minimization and curve-fitting for python. URL: <https://zenodo.org/record/11813>, doi:10.5281/ZENODO.11813.
- [27] Pai, D.K., Rothwell, A., Wyder-Hodge, P., Wick, A., Fan, Y., Larionov, E., Harrison, D., Raj Neog, D., Shing, C., 2018. The human touch: measuring contact with real human soft tissues. *ACM Trans. Graph* 37, 12. URL: <https://doi.org/10.1145/3197517.3201296>, doi:10.1145/3197517.3201296.
- [28] Schorr, S.B., Okamura, A.M., 2017. Three-dimensional skin deformation as force substitution: wearable device design and performance during haptic exploration of virtual environments. *IEEE Transactions on Haptics* 10, 418–430. doi:10.1109/TOH.2017.2672969.
- [29] Schwartz, D., Magen, Y.K., Levy, A., Gefen, A., 2018. Effects of humidity on skin friction against medical textiles as related to prevention of pressure injuries. *International Wound Journal* 15, 866–874. URL: <http://doi.wiley.com/10.1111/iwj.12937>, doi:10.1111/iwj.12937.
- [30] Sivamani, R.K., Goodman, J., Gitis, N.V., Maibach, H.I., 2003a. Friction coefficient of skin in real-time. *Skin Research and Technology* 9, 235–239. doi:10.1034/j.1600-0846.2003.20361.x.
- [31] Sivamani, R.K., Wu, G.C., Gitis, N.V., Maibach, H.I., 2003b. Tribological testing of skin products: gender, age, and ethnicity on the volar forearm. *Skin Research and Technology* 9, 299–305. URL: <http://doi.wiley.com/10.1034/j.1600-0846.2003.00034.x>, doi:10.1034/j.1600-0846.2003.00034.x.
- [32] Tang, W., Bhushan, B., Ge, S., 2010. Friction, adhesion and durability and influence of humidity on adhesion and surface charging of skin and various skin creams using atomic force microscopy. *Journal of Microscopy* 239, 99–116. URL: <http://doi.wiley.com/10.1111/j.1365-2818.2009.03362.x>, doi:10.1111/j.1365-2818.2009.03362.x.
- [33] Timm, K., Myant, C., Spikes, H.A., Schneider, M., Ladnorg, T., Grunze, M., 2011. Cosmetic powder suspensions in compliant, fingerprintlike contacts. *Biointerphases* 6, 126–134. URL: <http://avs.scitation.org/doi/10.1116/1.3640042>, doi:10.1116/1.3640042.
- [34] Tomlinson, S.E., Lewis, R., Carré, M.J., 2009. The effect of normal force and roughness on friction in human finger contact. *Wear* 267, 1311–1318. URL: <https://www.sciencedirect.com/science/article/pii/S0043164809001975>, doi:10.1016/J.WEAR.2008.12.084.
- [35] Veijgen, N.K., Masen, M.A., van der Heide, E., 2012. A novel approach to measuring the frictional behaviour of human skin in vivo. *Tribology International* 54, 38–41. URL: <http://dx.doi.org/10.1016/j.triboint.2012.05.022>, doi:10.1016/j.triboint.2012.05.022.
- [36] Vilhena, L., Ramalho, A., 2016. Friction of human skin against different fabrics for medical use. *Lubricants* 4, 1–10. URL: <http://www.mdpi.com/2075-4442/4/1/6>, doi:10.3390/lubricants4010006.
- [37] Wiertelowski, M., Hudin, C., Hayward, V., 2011. On the 1/f noise and non-integer harmonic decay of the interaction of a finger sliding on flat and sinusoidal surfaces. 2011 IEEE World Haptics Conference , 25–30doi:10.1109/WHC.2011.5945456.
- [38] Zhang, M., Mak, A.F.T., 1999. In vivo friction properties of human skin. *Prosthetics and Orthotics International* 23, 135–141. URL: <http://journals.sagepub.com/doi/pdf/10.3109/03093649909071625>, doi:10.3109/03093649909071625.
- [39] Zhu, Y.H., Song, S.P., Luo, W., Elias, P.M., Man, M.Q., 2011. Characterization of skin friction coefficient, and relationship to stratum corneum hydration in a normal Chinese population. *Skin Pharmacology and Physiology* 24, 81–86. URL: <http://pmc/articles/PMC2997446/>, doi:10.1159/000321993.